Electrochimica Acta 496 (2024) 144474

Contents lists available at ScienceDirect

Electrochimica Acta

journal homepage: www.journals.elsevier.com/electrochimica-acta

Machine learning-assisted equivalent circuit identification for dielectric spectroscopy of polymers

Bashar Albakri [a], Analice Turski Silva Diniz [b], Philipp Benner [a], Thilo Muth [a], Shinichi Nakajima [c,d,e], Marco Favaro [b], Alexander Kister [a,*]

[a] Section VP.1 eScience, Federal Institute for Materials Research and Testing (BAM), Unter den Eichen 87, 12205, Berlin, Germany
[b] Institute for Solar Fuels, Helmholtz-Zentrum Berlin für Materialien und Energie GmbH, Hahn-Meitner-Platz 1, 14109, Berlin, Germany
[c] Machine Learning Group, Technische Universität Berlin, 10587, Berlin, Germany
[d] Berlin Institute for the Foundations of Learning and Data, 10587, Berlin, Germany
[e] RIKEN Center for AIP, Tokyo 103-0027, Germany

ARTICLE INFO

Dataset link: https://github.com/BAMeScience/EISNet

Keywords:
Polymer membranes
Electrochemical impedance spectroscopy
Broadband dielectric spectroscopy
Deep learning
Machine learning
Equivalent circuit

ABSTRACT

Polymers have become indispensable across fields of application, and understanding their structure–property relationships and dynamic behaviour is essential for performance optimization. Polymer membranes, particularly ion exchange membranes, play a crucial role in renewable energy conversion technologies, fuel cells, solar energy conversion, and energy storage. In this context, broadband dielectric spectroscopy (BDS) offers a powerful, non-destructive approach to investigate the electrical response and relaxation dynamics of polymers. These properties are investigated by parametrizing the system's impedance response in terms of a network of circuit elements, i.e. the electrical equivalent circuit (EEC), whose impedance resembles the one of the system under investigation. However, the determination of the EEC from BDS data is challenging due to system complexity, interdependencies of circuit elements, and researcher biases. In this work, we propose a novel approach that incorporates a convolutional neural network (CNN) model to predict the EEC topology. By reducing user bias and enhancing data analysis, this approach aims to make BDS accessible to both experienced users and those with limited expertise. We show that the combination of machine learning and BDS provides valuable insights into the dynamic behaviour of polymer membranes, thus facilitating the design and characterization of tailored polymers for various applications. We also show that our model outperforms state-of-the-art machine learning methods with a top-5 accuracy of around 80% for predicting the circuit topology and a parameter fitting error as low as 0.05%.

1. Introduction

Polymers, with their diverse applications ranging from materials science to engineering and biotechnology, have become indispensable in our modern world. Understanding the structure–property relationships and dynamic behaviour of polymers is crucial for tailoring their properties and optimizing their performance. Among the many different polymer-based materials, polymer membranes have emerged as key components in various renewable energy conversion technologies, since they play a crucial role in facilitating the efficient generation, storage, and utilization of renewable energy, thus supporting new avenues for a clean and sustainable future. Polymer membranes, commonly known as ion exchange membranes (IEMs), are at the heart of fuel cells. These devices convert the chemical energy of a fuel, such as hydrogen or methanol, into electrical energy through an electrochemical reaction. IEMs enable the selective transport of protons while blocking the passage of electrons, facilitating the controlled flow of ions necessary for fuel cell operation. The high ion conductivity, excellent chemical stability, and mechanical flexibility of polymer membranes make them ideal for such applications, enabling the conversion of renewable fuels into electricity with minimal environmental impact [1,2]. Solar energy conversion technologies, such as solar fuel production, rely on IEMs as well to enhance their efficiency and functionality. Photoelectrochemical cells convert the energy from sunlight into chemical energy through electrochemical reactions, such as water splitting or oxidation of biomass analogs [3,4], resulting in the production of green hydrogen. In these devices, IEMs are used to separate the electrooxidation and hydrogen evolution half-reactions, allowing for efficient and cost-effective solar-driven reactions [5]. Similarly, in energy storage technologies such as batteries and supercapacitors, polymer membranes

* Corresponding author.
E-mail addresses: marco.favaro@helmholtz-berlin.de (M. Favaro), alexander.kister@bam.de (A. Kister).

https://doi.org/10.1016/j.electacta.2024.144474
Received 30 January 2024; Received in revised form 22 April 2024; Accepted 19 May 2024
Available online 25 May 2024

separate and facilitate ion transport between electrodes, ensuring high energy and power densities [6,7]. Additionally, polymer membranes find application in emerging energy conversion technologies, such as electrochemical water desalination, where they enable the selective transport of ions for water purification [8].

Among the various characterization techniques developed for the investigation of polymers, broadband dielectric spectroscopy (BDS) constitutes a powerful tool for probing the electrical response and relaxation dynamics of polymers over a wide range of frequencies and temperatures [2]. BDS offers a non-destructive and non-invasive approach to studying polymers, allowing for in situ measurements under realistic working conditions. This capability is particularly valuable for investigating the behaviour of polymers in complex environments, such as during processing, under mechanical stress, or in the presence of solvents or additives. By monitoring the dielectric response in these situations, BDS provides insights into how external factors influence the molecular dynamics and electrical properties of polymers, facilitating the development of advanced materials with enhanced functionality and stability. Moreover, BDS enables capturing the dynamic response of polymers across multiple frequency scales: the polymers' dielectric response is investigated as a function of AC voltage or current signals from low (typically below a mHz) to high frequencies (up to a few GHz). If the amplitude of the AC signal is small enough, the input and output AC signals have the same frequency (within the control theory the system under investigation is categorized as Linear, Time-Invariant, or LTI) [9]. Under the linearity and time-invariance conditions, the output AC signal will be detuned with respect to the input signal, meaning that a phase (time) shift exists between the two AC signals. This phase shift, known as system transfer function when operating in the frequency domain, contains information about the response of the polymer to the feeding AC signal and is investigated by parametrizing the system's impedance response in terms of a network of circuit elements, such as resistors, capacitors, and Warburg elements [10]. The topology and element values of this electrical equivalent circuit (EEC) reveal information about the response processes occurring in the polymer [2]. By fitting the experimental impedance data to an appropriate EEC [11], it is possible to extract quantitative parameters that characterize these properties. Polymeric materials often exhibit multiple relaxation processes or contributions from different types of charge carriers. The electrical equivalent circuit helps in modelling such complex systems by incorporating different circuit elements to represent the various relaxation mechanisms or charge transport pathways. This enables a more accurate representation of the system's behaviour and facilitates the analysis of multiple dynamic processes occurring simultaneously. Additionally, the relaxation processes observed in BDS can provide insights into the molecular dynamics and intermolecular interactions within the material. The EEC helps in isolating and characterizing these relaxation processes by assigning specific circuit elements to represent the corresponding physical phenomena. By correctly identifying and quantifying these processes, it becomes possible to study different phenomena in polymeric materials such as glass transitions, segmental dynamics, dipolar relaxations, and ion transport [2,12]. Despite the importance of obtaining the correct EEC, its determination can be challenging due to several factors [12]:

- Complex systems often exhibit overlapping relaxation processes or non-ideal behaviours, making it difficult to identify the appropriate circuit elements that represent the underlying physics. Decoupling the contributions from different relaxation mechanisms and accurately modelling their behaviour requires careful consideration and expertise;
- The available experimental data may be insufficient to fully capture the system's complexity or resolve subtle features. Insufficient frequency range typically makes it challenging to identify the correct EEC;
- Within the EEC, circuit elements usually exhibit interdependencies, leading to correlations between the extracted parameters. This makes it challenging to uniquely determine the values of individual circuit elements without ambiguity.
- Finally, and perhaps most importantly: researchers may have preconceived notions or biases when selecting the model or circuit elements for fitting the experimental data. This can inadvertently influence the interpretation of the results and lead to inaccurate or oversimplified representations of the system.

Overcoming these challenges requires a combination of experimental expertise, theoretical understanding, and careful data analysis. Iterative approaches, model comparisons, and validation with independent measurements can help refine the electrical equivalent circuit and improve its accuracy in representing the electrical behaviour of the system under investigation in BDS. This comprehensive understanding of the dynamic behaviour is crucial for designing polymer materials with tailored properties and predicting their performance under different conditions.

So far, the standard procedure for retrieving the EEC consists of two stages: In the first stage an educated guess for the EEC topology is made, where the topology specifies the types (resistor, capacitor, ...) of the elementary parts (circuit elements) as well as the way these parts are connected. In the second stage, the parameters of the circuit elements are optimized by fitting the corresponding circuit transfer function to the measured impedance spectra. The fitting is performed by employing minimization methods such as the least mean square or non-linear least squares which utilize finite difference methods for gradient estimation [13–15]. The goodness of fit and the physical meaning of the retrieved circuit element values are used to validate the choice of the particular EEC topology selected in the first stage to interpret and fit the experimental data. Generally, it is common to iterate multiple times through the two aforementioned steps modifying each time the guess in the first stage, until the fitting with the experimental data reaches a satisfactory degree. Clearly, this procedure strongly relies on the experience of the experimenter, and it is affected by the biased choice of the EEC topology. In this work, we describe a new procedure where we replace the educated guess of the EEC topology in the first stage with a prediction of a machine learning algorithm. Our aim is to reduce the user's bias in the BDS data analysis, thereby helping the expert BDS users to extract valuable information from their experimental data, and to make BDS accessible to experimenters with limited experience as well.

2. Related work

2.1. Experimental setup

The sample cell geometry for BDS investigations reported in the literature depends on various factors, such as the nature of the sample and its surrounding environment, measurement requirements [2,16], and the desired information about the sample's electrical properties. Commonly used cell geometries in BDS are the following [2]:

- Parallel Plate Geometry: The parallel plate geometry is the most straightforward and widely used configuration. It consists of two flat and parallel electrodes with the sample placed between them. This geometry is suitable for measuring bulk samples or thin films. The electrode spacing can be adjusted to control the electric field strength and focus on specific sample regions.
- Interdigitated Electrodes: Interdigitated electrodes (IDE) are designed as an array of closely spaced and alternating fingers. The sample is placed between these fingers, allowing for a more localized measurement of the electrical properties. IDE configurations are particularly useful for studying thin films, powders, and porous materials. They provide a larger surface area and promote enhanced electric field penetration.

- Cylindrical Geometry: In cylindrical geometry, the sample is in the form of a cylindrical shape. The electrodes can be concentric cylinders or discs placed at the ends of the sample. This geometry is suitable for investigating materials with cylindrical symmetry or when measurements along the radial direction are of interest. Cylindrical cells are often used for studying liquids, gels, or biological samples.
- Transmission Line Geometry: The transmission line geometry involves embedding the sample within a transmission line structure, such as a coaxial cable or microstrip line. The electrical properties of the sample are determined by measuring the impedance changes along the transmission line. This geometry is advantageous for studying thin films, coatings, or materials with limited sample volumes.
- Microfluidic Cells: Microfluidic cells are designed for BDS measurements on small volumes of liquids or solutions. They often feature microchannels or microcapillaries where the sample flows continuously. Microfluidic cells offer precise control of sample flow, including fast switching of experimental conditions and sample environment [17], enabling investigations of processes occurring within a wide dynamic range.
- Cells for Local Electrochemical Impedance Spectroscopy (LEIS): Electrochemical systems may exhibit non-ideal behaviour across macroscopic samples, making data interpretation difficult for surface-averaged techniques. To overcome these challenges, scanning techniques utilizing metal microelectrodes have been developed over the years. LEIS is a powerful tool for exploring electrode heterogeneity and is rooted in the development of electrochemical techniques employing microelectrode scanning [18,19]. This technique detects local impedance by measuring the AC-local current density near the working electrode in a typical three-electrode cell configuration [18,19]. It utilizes a dual microelectrode mounted on a three degrees-of-freedom manipulator to sense the local AC-potential gradient, with the local current calculated using Ohm's law. Studies have shown that lateral resolutions of few tens of mm can be achieved using such an experimental geometry [19].

2.2. Machine learning approaches in electrochemical impedance spectroscopy

All existing machine learning approaches for finding an equivalent circuit follow a two-stage approach. First, they predict the circuit topology. Second, they employ an optimization algorithm for finding the parameters of the electrical elements of the predicted circuit. The topology prediction task is formulated as a supervised classification task, therefore the set of all possible topologies, which in principle has infinitely many members, is restricted to a problem-dependent subset of candidate typologies.

Collecting a data set of impedance measurements labelled with the topology is expensive. Therefore, it is common to use simulations for generating the training dataset [20–23]. To generate the dataset, an assumption on the distribution of the data must be made. For instance, some studies rely on a uniform distribution [20,23] due to the lack of prior on the true distribution of the real data, whereas others choose a Gaussian distribution [22] for the data generation. However, it was shown [23] that a uniform distribution helps models achieve better accuracy on real data.

The heterogeneity of the concrete application domains (corrosion analysis, batteries, polymers, etc.) leads to different sets of candidate topologies. This makes it hard to compare the performances of the different approaches. Most of these different candidate sets include topologies that contain, in addition to further domain-dependent elements, up to three different RC circuits connected in series [20–23].

For certain candidate sets the task of identifying the topology can be done by visual inspection. For example, in the absence of additional domain-dependent elements, visually identifying the number of RC elements, under suitable restriction on the parameters of the RC elements, is possible: if the products of the resistance R and the capacitance C (also called time constant) of the distinct RCs are far enough apart, each RC element corresponds to a semi-circle in the so-called Nyquist plot. If the time constants of the two RCs are too close, the semi-circles are overlayed and cannot be distinguished by visual inspection. The feature of the presence or absence of a semi-circle is an indicator of the presence or absence of an RC element independent of its location in the Nyquist plot.

There exists a machine learning approach [25] that mimics this visual inspection by converting impedance data to images of Nyquist plots and uses a CNN to predict the topology from the images. The impedance-to-image approach did not perform as well as methods (published in the same paper) that processed the data in tabular form. One reason for this underperformance is the neglect of the impedance's magnitude. The magnitudinal progression in temporal sequences of the impedance data cannot be precisely observed in images. Another reason that also affects the performance is that frequency-dependent features cannot be examined visually.

Overall the existing work shows that also on the tabular data, more complex models are necessary: AdaBoost has better performance than Logistic regression [21], an SVM with RBF kernel performs better than one with linear kernel [21], a fully connected neuronal network with four layers had a better performance than networks with fewer layers [20], which can be explained by the nonlinearity of the problem, in addition to the fact that the data is abundant which allows complex models to be easily fitted.

Machine learning is also used to speed up the second step, in which the optimal parameters of the electrical elements are determined. This step is either completely replaced by a machine learning model [20] or machine learning is used to predict an initial set of parameters that is refined by gradient descent methods [23].

However, the problem in these approaches is that the circuit topology must be fixed [20] or partly fixed [23], meaning for each circuit topology an independent model (neural network) is trained to estimate the parameters of a specific circuit which is expensive. A possible improvement for this approach was proposed by Buteu et al. [23] by adding a regularization term to the loss function that penalizes unnecessary RCs during the fitting procedure. However, elements in the circuit other than the RCs stay fixed without a penalty term which makes the topology partly fixed. In our approach, we use a CNN model for predicting the circuit topology with tabular impedance data. Subsequently, we use a global optimization algorithm, the multi-start Trust Region method, for the parameter fitting which turns out to be sufficient (with a very low fitting error) and has the advantage of being applicable to any possible topology without the need for training.

3. Experimental section

3.1. Membranes

We investigated two ion exchange membranes in this study: a commercially available cationic exchange membrane (referred to as Nafion® N115, Alfa Aesar) and an anionic exchange membrane (referred to as Fumasep® FAA-3-PK-75, purchased in bromide and dry form from Fumatech, GmbH). Both types of membranes were received as 30 × 30 cm^2 sheets and then cut into (20 ±0.5) mm diameter discs using a stainless steel puncher. Prior to conducting the experiments, the membranes underwent a cleaning and activation procedure following specific protocols, as reported in our previous work.[26] For the Nafion® N115 membranes, thorough rinsing with Milli-Q® ultrapure water (resistivity 18.2 MΩ·cm at 25 °C, total organic carbon (TOC) ≤5 ppb) was performed, followed by sonication in Milli-Q® water for

Table 1
Overview of state-of-the-art machine learning applications in EIS for different application domains.

Authors	Classification model	Data type	Application domain	Target circuits	Accuracy
Bongiorno et al. [20]	FCNN	Tabular	Corrosion	-Three circuits (scenario 1) -Three circuits (scenario 2)	95% 75%
Zhao et al. [21]	RF[a]	Tabullar	Batteries and Supercapacitors	Nine circuits	58.2%
Zhao et al. [24]	SVM	Tabular	Batteries and Supercapacitors	Five circuits	78%
Al-Ali et al. [22]	CNN-LSTM	Tabular	Batteries	−20 single depression circuits −10 double depression circuits	82.8% 60%
Schaeffer et al. [25]	-XGBoost[b] -CNN	Tabular Image	Batteries	Nine circuits	50% 32%

[a] The authors benchmark multiple models on the same circuits and data, where Random Forest achieves the best accuracy.
[b] The authors benchmark XGBoost with Random Forest on the tabular data. XGBoost shows better performance.

10 min. Subsequently, the membrane was left in an aqueous solution of hydrogen peroxide (H_2O_2 : H_2O 30%, Carl Roth GmbH + Co. KG) at room temperature (r. t., 21 °C) with continuous stirring to oxidize and remove potentially remaining metal polymerization starters, such as Cesium. After rinsing the membrane with Milli-Q® water, it was immersed in a 1.0 M aqueous solution of sulfuric acid (H_2SO_4, 97%, Honeywell, Fluka) and heated to its boiling point under stirring and reflux for one hour to further remove impurities and activate the membrane through proton pumping. Following the cooling of the solution to at least 40 °C, the membranes were removed, washed copiously with Milli-Q® water, and then stored in an aqueous solution of H_2SO_4 (50 mM). Borosilicate glassware (Schott) was used throughout the cleaning, activation, and storage processes to handle the Nafion® N115 membranes. For the Fumasep® FAA-3-PK-75 samples, the same initial rinsing and sonication with Milli-Q® water were conducted. The membranes were briefly dipped in an aqueous hydrogen peroxide solution (H_2O_2 : H_2O 30%) at r. t., and then soaked in a 0.5 M aqueous solution of sodium hydroxide (NaOH, diluted from 1.0 M solution, Honeywell, Fluka) at r. t. with continuous stirring for one hour (hydroxide pumping). The membranes were then removed from the NaOH solution, thoroughly washed with Milli-Q® water, and stored in an aqueous solution of NaOH (100 mM) until use. To prevent extensive Si contamination from silica leaching in base environments, high-density polyethylene (HDPE) lab ware (Thermo Fisher Scientific Nalgene®) was utilized for both cleaning/activation and storage of the Fumasep® FAA-3-PK-75 membranes. Each run of the described protocols allowed for cleaning, activation, and storage of five membrane discs. Before their investigation, the membrane samples were removed from their storing solutions, thoroughly rinsed with Milli-Q® water, and gently dried between clean, lint-free precision wipes (Precision Lens Cleaning Wipes, 304 × 304 mm, Science Service).

3.2. Experimental setup

Four-terminal sensing (4T sensing) or 4-point probes method (also known as Kelvin sensing or connection) is an electrical impedance measuring technique that uses separate pairs of current-carrying and voltage-sensing electrodes to make more accurate measurements than usual two-terminal (2T) sensing. The separation of current and voltage electrodes eliminates the lead and contact resistance from the measurement. This is an advantage for precise measurement of low resistance values.

The experimental impedance spectra reported in this work were taken in a Kelvin-configured setup, in galvanostatic mode (i.e. constant current fixed at a desired setpoint), at a current of 100 μA, and a current range of 1 mA. The current and potential signals during the experiments were generated and monitored using a potentiostat/galvanostat/frequency response analyser FRA (VSP-300, Biologic). The potentiostat's bandwidth was set to 1 kHz (time constant of 1 ms). The potentiostat was controlled with the EC-Lab® software (Biologic, V11.34). The AC amplitude of the current signal was equal to ±5 μA (10 μA total amplitude), while the frequency range was 1 MHz–50 mHz. The current was supplied via a pair of platinum (platinum foil, Alfa Aesar, 011508.FI Premion, 0.25 mm thick, 99.99%) force connections (current leads or power electrodes) generating a voltage drop across the membrane, whose impedance is thus measured according to the generalized Ohm's law ($V = I \cdot Z$). A second pair of independent sense connections (voltage drop probes) were brought in contact with the membrane sample through the circular aperture on the cell cap (Ø = 12.0mm), measuring the voltage drop generated by the current flowing through the power electrodes. Since almost no current flows through the sense leads the corresponding voltage drop is negligible, allowing them to measure the "true" impedance (Z) across the polymer membrane. The measurements were performed at room temperature (about 21 °C) and pressure, and at a relative humidity (RH) ranging between 60 and 70% in order to prevent the membranes from drying. The temperature and RH values were logged throughout the experiments using a local probe (TSP01-TH, Thorlabs), placed in close proximity to the sample under investigation.

The voltage drop probes were Pt tips with a diameter of 1 mm obtained from Pt rods (Goodfellow, PT00-RD-000120, diameter 2.0 mm, length 10 mm, 99.95%). The contact area between the probes and the membrane was kept low (0.8 mm2) to suppress interfacial resistances, as shown in Figs. 1 and 2 (reporting digital photographs of the experimental setup and a schematization of the electrical connections, respectively). The probes were brought in contact with the membrane by means of an xyz manipulator (see Fig. 1c).

The *z*-axis of the manipulator was customized to include a torque control system, to ensure a reproducible and reliable pressure of the probes on the membrane under investigation. The applied torque M was equal to 0.05 N m. Note that M = F·R, where F is the applied force and R is the radius of the tip (0.5 mm). Hence, the force applied by one probe to the membrane can be determined as follows: F = M/R = 100 N (10.19 kg-force). The clamping pressure exerted by one voltage drop probe on the membrane was therefore equal to about 127 MPa. The membrane sample was pressed by a Nylon and a μ-metal® washer (fabricated from a foil, Magnetic Shield Corp., MU012-12, uncoated, 0.305 mm thick). The latter, grounded to the Earth ground, ensured a minimization of the electromagnetic interference caused by the AC current signal fed to the power electrodes on the voltage drop probes. A second stainless steel Faraday cage encased the overall BDS experimental setup, providing electromagnetic shielding by blocking external electromagnetic interference.

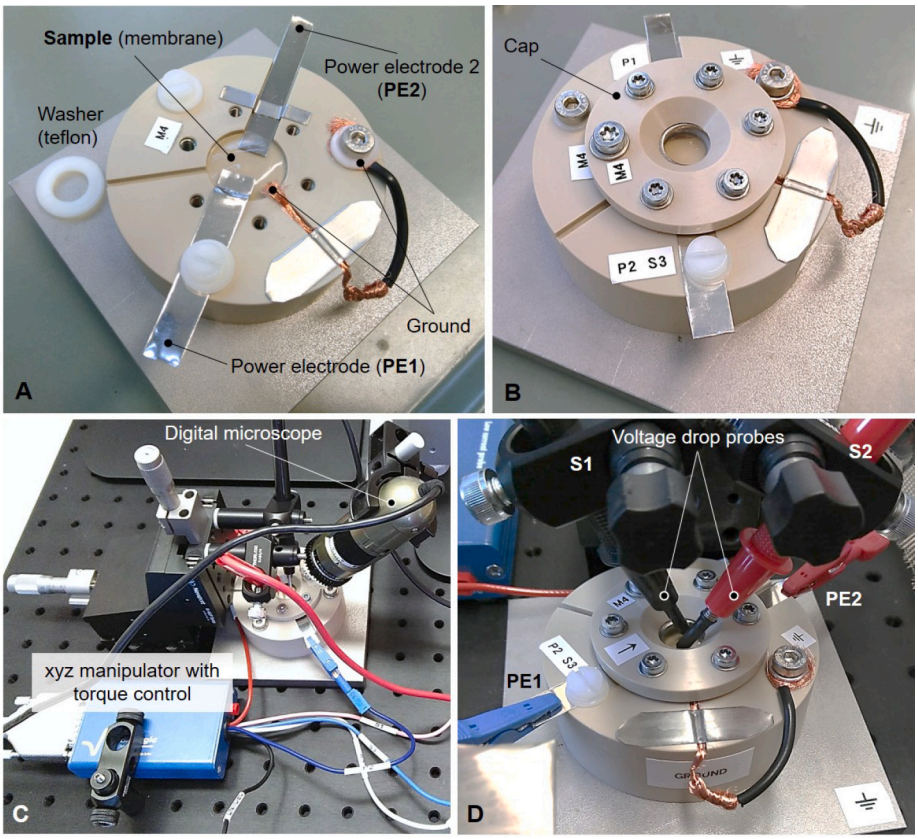

Fig. 1. Digital photographs of the broadband dielectric spectroscopy (BDS) setup developed at the Institute for Solar Fuels of the Helmholtz Zentrum Berlin. A, B: details of the membrane holder; C, D: details of the setup during measurements. It is possible to see the voltage drop probes contacting the top surface of the membrane sample for the determination of the voltage drop across it, as a function of the fed AC current signal to the power electrodes.

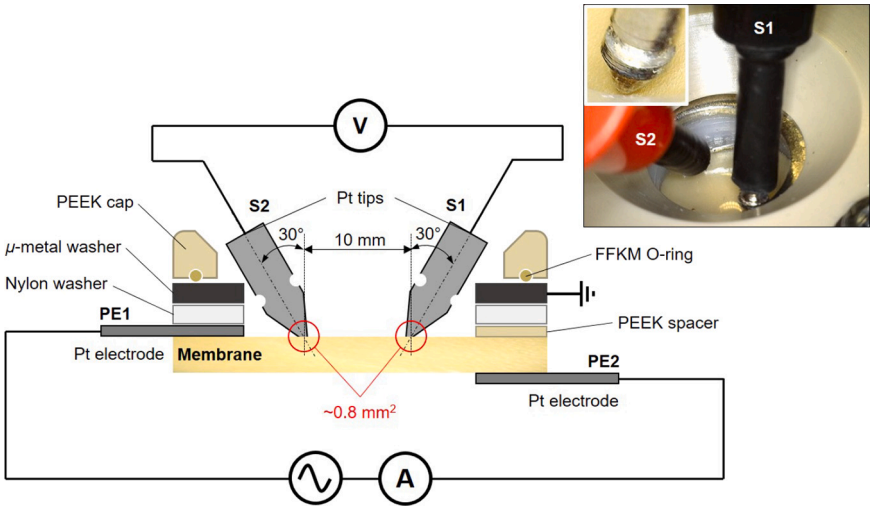

Fig. 2. Schematic of the Kelvin configuration used to measure the sheet resistance of polymer membranes.

4. Machine learning approach for determining the equivalent electrical circuit

The goal of our machine learning model is to approximate the function, which maps impedance data to an electrical circuit that has an equivalent impedance.

We utilize a two-step methodology to determine the electrical circuit. In the first step, we employ a neural network to determine the topology of the electrical circuit. We use supervised learning, which is an approach in machine learning where a model is trained on labelled data, meaning it learns the map from provided inputs (impedance) to their corresponding outputs (topology). In the second step, we use a global optimization method to determine the parameters of the

electrical elements of this previously predicted circuit. We describe in Section 4.1 how the training data is generated. Furthermore, the neural network model and the global optimization method are detailed in Section 4.2.

4.1. Data generation

Each entry in the training set corresponds to an electrical circuit. These entries are pairs consisting of the impedance data (the input of the learned model) and the description of the electrical circuit (the desired model output). An electrical circuit can be described by the topology of the circuit and the parameters, however, for training the neural network, we only require the topology of the electrical circuit. To obtain a diverse training set, we pick a set of electrical circuits randomly. This is done in two steps: first, we generate the circuit topology and afterwards, we generate the parameters of the electrical elements. To obtain the corresponding impedance data, we use Kirchoff's rules that imply an explicit formula for the impedance (see Eq. (1)).

Step 1: Generating the topology

As it is common in literature (see Table 1), we select a finite set of possible candidate topologies. These topologies are certain sub-circuits of a circuit that we call a universal circuit (see Fig. 3). The set of sub-circuits of the universal circuit can model most of the EECs encountered in EIS. To obtain the candidate circuits, certain sets of elements are removed from the universal circuit: We represent the topology by a vector of binary variables $B_{elem} = [B_{c_s}, B_{l_s}, B_w, B_{p_1}, B_{p_2}]$ and the integer-valued variable $N_{RC} \in \{0, 1, 2\}$, where N_{RC} denotes the number of RCs in series. B_{elem} corresponds to the presence or absence of the electrical circuit elements highlighted in the coloured boxes in Fig. 3. If a variable in the binary vector has the value one, it means that the corresponding element is present in the circuit. Hence, we restrict ourselves to $3\times2^5 = 96$ different circuits, since N_{RC} is restricted to three values and there are five binary variables in B_{elem}. The smallest possible subcircuit is an RC circuit connected to the series resistance R_s.

To randomly generate a topology, we sample the elements of B_{elem} from a Bernoulli distribution (see Table 2 for parameters of the Bernoulli distribution) and the number of RCs, N_{RC}, from a uniform distribution over $\{0, 1, 2\}$.

Step 2: Generating the parameters of the elements

Once the topology is specified we randomly choose the parameters of the elements. These parameters are generated from a uniform distribution over the intervals specified in Table 2. These intervals represent practical values that can be experimentally explored when performing EIS on energy-related systems (i.e. not only on polymer membranes, but also on metal/, oxide/, and semiconductor/liquid electrolyte interfaces). These values and their variability ranges have been selected based on the practical experience in EIS experiments and from data reported in the literature, in particular in the works of Bredar et al. [27], Vivier et al. [10], and Lazanas et al. [12].

Generating the impedance data

To generate the impedance data, we use Kirchhoff's rules. The impedance of the universal circuit (and its sub-circuits) is determined by the impedance of each element:

$$Z = Z_{R_s} + B_{c_s} Z_{c_s} + B_{l_s} Z_{l_s} + Z_{RC_m} + \sum_{k=1}^{N_{RC}} Z_{RC_k}, \tag{1}$$

where,

$$Z_{RC_m} = \frac{1}{\frac{1}{Z_{c_1}} + \frac{1}{Z_{R_1} + \frac{B_{p1}}{\frac{1}{Z_{C_p}} + \frac{1}{Z_{R_{p1}}}} + B_w Z_w} + \frac{B_{p_2}}{Z_{R_{P2}} + Z_{L_p}}} \tag{2}$$

The frequency dependence of the impedance of the single electrical elements is not explicitly highlighted in the notation. To obtain the impedance spectra, Eq. (1) is applied for multiple frequencies.

Table 2
Parameter distribution during data generation. This table presents the distribution of parameters employed in shaping the circuit impedance model (Eq. (1)), with the associated binary values displayed in the 'Random Variables' column, along with their respective probabilities on the right side. The table also shows the parameter distribution of the electrical elements sampled from a uniform distribution with the lower and upper bounds specified in the table.

Element	Lower bound	Upper bound	Random variable	Probability
R_s	1×10^{1}	1×10^{6}	–	1
C_s	1×10^{-7}	1×10^{-4}	B_{C_s}	0.2
L_s	1×10^{-6}	2×10^{-4}	B_{L_s}	0.2
W	80	160	B_w	0.5
R_1	1×10^{1}	1×10^{6}	$N_{RC} = 0$	$\frac{1}{3}$
C_1	1×10^{-7}	1×10^{-4}	$N_{RC} = 0$	$\frac{1}{3}$
R_{p1}	1×10^{1}	1×10^{6}	B_{p1}	0.5
C_p	1×10^{-7}	1×10^{-4}	B_{p1}	0.5
R_{p2}	1×10^{1}	1×10^{6}	B_{p2}	0.5
L_p	1×10^{-6}	2×10^{-4}	B_{p2}	0.5
R_2	1×10^{1}	1×10^{6}	$N_{RC} = 1$	$\frac{1}{3}$
C_2	1×10^{-7}	1×10^{-4}	$N_{RC} = 1$	$\frac{1}{3}$
R_3	1×10^{1}	1×10^{6}	$N_{RC} = 2$	$\frac{1}{3}$
C_3	1×10^{-7}	1×10^{-4}	$N_{RC} = 2$	$\frac{1}{3}$

While Eq. (1) allows us to determine the impedance for any frequency, the measurements are only done for a discrete set of frequencies. In the training set, the spectra consist of $n = 200$ frequency points, where the corresponding 200 frequencies are taken at equally spaced (on the logarithmic scale) points within the interval $[10^{-3}, 10^{8}]$.

The impedance spectrum is represented by a 2×200 dimensional matrix, where the rows correspond to the real and imaginary part of the impedance. The choice of the number n of measurement points for the frequency is based on two criteria. The first criterion is the measurement time. For example, measuring the impedance at the frequency 10^{-3} Hz, leads to a measurement time of $\frac{1}{10^{-3}} = 1000$ seconds. Therefore the lower bound of the frequency interval should not be too small. The second criterion is the loss of information. The smaller the number of measurement points the more features we lose.

4.2. Model

4.2.1. Classification model: neural network

We represent the impedance spectra by a $2\times n$ dimensional matrix Z, where the two rows correspond to the real and the imaginary parts $Z = [Z_r^T, -Z_i^T]^T$, and the columns correspond to the frequency information. The frequency vector is not explicitly passed to the network as an input since the frequency grid is fixed. Therefore, the network learns features related to the frequency based on the positions of the inputs. We employ a 2D CNN for the classification task. In contrast to 1D CNNs, where the imaginary part and real part are passed to the input layer in the form of two different channels, we pass them as 2D input to a 2D CNN with shared kernels. This is because the real and imaginary parts of the impedance are in fact interdependent as shown in the Kramers–Kronig equations [28]. The architecture of the developed CNN can be seen in Fig. 4.

The impedance data has multi-scale features: For instance, when the capacitor in series (C_s) is present, it results in an exponential impedance curve which has a larger order of magnitude compared to the impedance of the other elements of the circuit. Such multi-scale features can affect the performance of the neural network negatively when directly standardizing the data due to the loss of some features at these frequencies. To avoid this, we transform the impedance data in a nonlinear manner by taking the logarithm of the data, and subsequently, we standardize the data. The standardization function can be seen in Eq. (3). This function was applied to the real and the imaginary part independently. We define the function as:

$$f(Z) = H(G(Z)), \tag{3}$$

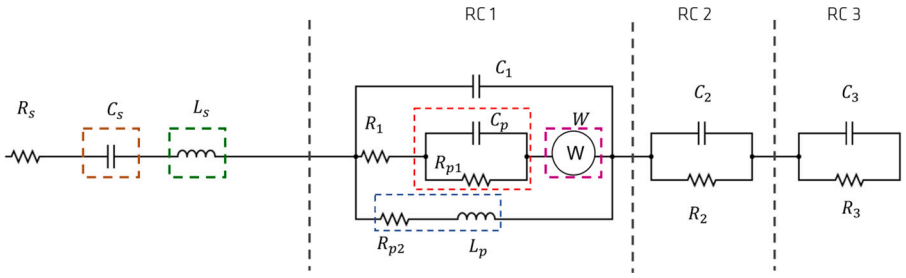

Fig. 3. The universal circuit is used to define the set of all circuits that we consider to be candidates for being the topology of an equivalent circuit: This circuit consists of 3 RCs in series, a series resistor R_s, a series capacitor C_S, a series inductor L_s, a Warburg element W, a parallel RC $R_{P_1} - C_p$, and a parallel RL $R_{P_2} - L_p$. An electrical circuit is an element of the candidate set if it can be derived from the universal circuit by dropping one or more of the mentioned elements (the ones that are highlighted by the dashed boxes) and/or by limiting the number of RCs to one, two or three.

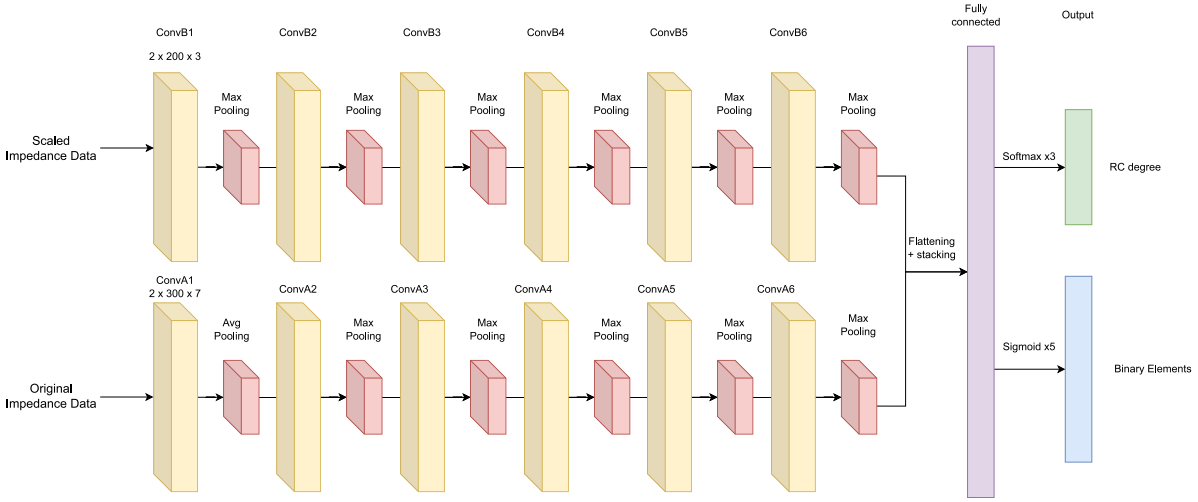

Fig. 4. Convolutional neural network architecture. The neural network is structured with two branches, each processing input data at different scales. This design allows learning features at different scales (scaled and non-scaled data).

where,

$$G(Z) = \log(Z + C) \tag{4}$$

$$H(x) = \frac{x - \mu}{\sigma} \tag{5}$$

and C is a constant added to whole impedance data to shift it such that we only have non-negative values. μ and σ are the mean and the standard deviation of the impedance after applying the logarithm. This pre-processing step is then done for any data point that we input to the neural network.

However, scaling the data might cause difficulties in learning some features. Therefore, we propose a multi-branch CNN, where one branch takes the scaled data as input and another takes the non-scaled data as input. This approach is motivated by the observation that there are patterns that can be detected with simple kernels in the scaled data and only with more complex kernels in the non-scaled data and vice versa. For example, the impedance of a Resistance is a constant function in the non-scaled data, which can be identified with a kernel that is sensitive to constant inputs. On the other hand, the real part of the impedance of a Warburg element is proportional to $1/\sqrt{(\omega)}$, which cannot be identified by a single kernel defined for the whole range of frequencies (instead we need a different kernel for each frequency range). Since the standard deviation of the real and imaginary part of the impedance is not constant over all frequencies, it is a function of the frequency, where the real part of this function has an inverse proportionality to the frequency ω similar to Warburg. Hence, scaling turns the data of the Warburg element into an approximately constant, and hence simple to identify the function. For the Resistance, scaling has the reverse effect.

Each branch consists of six 2D convolutional layers with kernel sizes of 1×3 and 1×7 on the input for branches 1 and 2 respectively. Moreover, each convolutional layer is followed by a pooling layer. The pooling layer is applied on each dimension separately. At the end of convolutional layers, the output of each branch is flattened and stacked to one vector to be passed to a dense layer and subsequently passed to the final output.

The output consists of two different layers. The first layer outputs a prediction $\hat{B}_{RC}$ for the number of the RCs in series, N_{RC}. $\hat{B}_{RC}$ has the form of a probability distribution over $\{0, 1, 2\}$, which represents the probabilities for each possible value of N_{RC}. To obtain this prediction we use a softmax layer. To find the predicted value of $\hat{N}_{RC}$, we take the argmax of $\hat{B}_{RC}$ (the index with the highest probability).

The second layer predicts the binary vector B_{elem}. This prediction, $\hat{B}_{elem}$, is a vector of probabilities of the corresponding variable being equal to one, which is implemented by a Sigmoid layer.

For the hidden layers of the neural network, we use a Tanh activation function, which in our case shows a better performance than the ReLU activation.

To optimize the parameters of the neural network we minimize the cross-entropy loss,

$$\begin{aligned}\text{Loss} = &\underbrace{-\frac{1}{3}\sum_{i=1}^{3} B_{RC_i} \cdot \log \hat{B}_{RC_i}}_{\text{RC Degree}} \\ &\underbrace{-\frac{1}{5}\sum_{i=1}^{5} B_{elem_i} \cdot \log \hat{B}_{elem_i} + \left(1 - B_{elem_i}\right) \cdot \log\left(1 - \hat{B}_{elem_i}\right)}_{\text{Binary Elements}},\end{aligned} \tag{6}$$

where the number of RCs, N_{RC}, is encoded as a one-hot vector B_{RC} taking values $\{[1,0,0]^T, [0,1,0]^T, [0,0,1]^T\}$.

4.2.2. Regression model: multi-start trust region optimization

We acquire a predicted circuit topology from the classifier (the neural network). To find its parameters, we optimize the circuit parameters such that the impedance spectrum of the optimized circuit fits as good as possible to the observed one, $(Z^{(k)}_{data})_{k\in\{1,\dots,n\}} = ((Z^{(k)}_{r,data}, Z^{(k)}_{r,data}))_{k\in\{1,\dots,n\}}$. During this optimization, we make sure that the fitted parameters are still within the bounds defined in Table 2. In other words, we have to solve the constrained optimization problem given by:

$$\min_{\theta} \quad \frac{1}{n}\sum_{k}^{n}[(Z^{(k)}_{r,model}(\omega_k,\theta) - Z^{(k)}_{r,data})^2 + (Z^{(k)}_{i,model}(\omega_k,\theta) - Z^{(k)}_{i,data})^2] \tag{7}$$
$$\text{s.t.} \quad \theta_{lb} \le \theta \le \theta_{ub},$$

where θ refers to the circuit parameters and ω is the angular frequency.

To solve the optimization problem shown in Eq. (7), we use the Trust Region method [13–15] as implemented in the SciPy library [29].

However, since the optimization problem is a non-convex problem, the Trust Region method is at risk of falling into a bad local minimum. To avoid this, we use the multi-start method: we solve the Trust Region optimizer at multiple random starting points (initiations).

Subsequently, we choose the parameters set with the lowest fitting error from the sets of parameters found at different initiations. In Section 5, we will show that this approach gives sufficiently good solutions and parameterization.

5. Results and discussion

We evaluate the performance of our model with regard to its performance in identifying the circuit topology and with regard to its ability to find an equivalent circuit (which includes not only finding the topology but also the parameters of the elements). A dataset of size 3×10^6 was generated. The dataset was split into 70% training, 20% validation, and 10% test dataset. The impedance spectra were generated at 200 frequencies within the interval $f \in [10^{-3}, 10^8]$. The neural network was trained with Adam optimizer for around 300 epochs with a batch size of 512 on a scheduled learning rate ranging from 10^{-4} to 10^{-6}.

5.1. Classification results

The classification results of the neural network for the presence or absence of each element of the universal circuit are given in Table 3.

Making the assumption that the Bernoulli variables are independent, we use the product of their likelihoods, which are given by $\hat{B}_{RC}$ and $\hat{B}_{elem}$, as the likelihood of the complete circuit. The chance that the circuit with the highest predicted likelihood is equal to the one that was used to generate the impedance spectra is around 40%. Fig. 5 shows the top-k accuracy, which is the chance that the circuit that was used to generate the topology is among the k circuits that have the highest predicted likelihood. We can see that the top-k accuracy grows very quickly (for increasing k) to 90%.

The low top-1 classification accuracy is explained by the fact that, for appropriately chosen parameters, two different circuit topologies can have highly similar or equal (this case is also known as non-identifiability) impedance spectra. The chance of observing such a problematic similarity is promoted by the large parameter space. Additionally, the accuracy is affected by the overlapping relaxation processes as mentioned in Section 1. For example, about 52% of the time, the neural network misclassifies the presence or absence of Warburg when the series capacitor is present. This is primarily due to the large exponential function that accompanies the series capacitor, which could override the impedance of the Warburg element and makes it difficult to detect. On the other hand, when there is no series capacitor the neural network fails to identify Warburg around 26% of the time. This is due to feature loss caused by large time constants and limited frequency range.

Table 3
Results table showing the performance of the neural network in the circuit prediction task on the test dataset.

Output	Recall	Precision	Accuracy
RC Degree	82% (averaged)	81% (averaged)	82%
C_s	100%	100%	100%
L_s	100%	100%	100%
W	68%	70%	69%
$R_{p1} - C_p$	80%	81%	80%
$R_{p2} - L_p$	79%	72%	75%

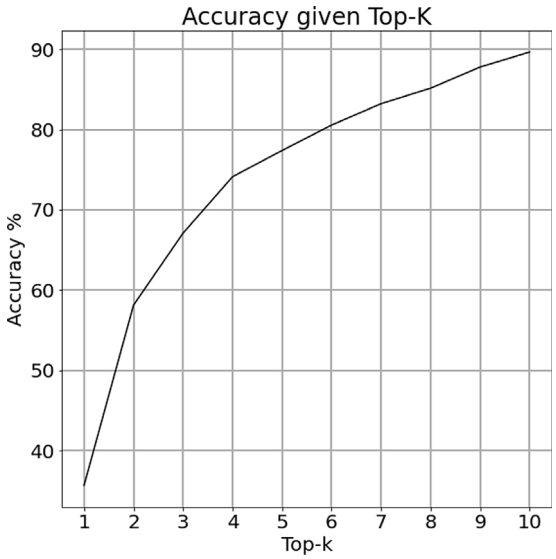

Fig. 5. The top-k accuracy for the top ten predictions. Top-k accuracy measures whether the true class is among the model's top-k predicted classes. The top ten predictions are the predictions of the neural network with the highest probability scores. The top-1 accuracy has a score of around 40% which is primarily due to non-identifiability in addition to the large number of target circuits. Conversely, the neural network has a top-5 accuracy of around 80%.

We benchmark our neural network model against some of the machine learning models mentioned in the related work section (Section 5.3). The models we chose to benchmark, are the models which have similar circuit models to our circuit model (Fig. 3). For this benchmarking, we train our model on the set of circuits that were used in the corresponding publication. The results are summarized in Table 4. Our model outperforms the proposed methods on top-1 prediction.

5.2. Regression results

By determining the goodness of fit we study two aspects of our model: we get an indication if the low top-1 prediction accuracy is caused by mathematical equivalence, and on the other hand we assess the predicted circuit (its topology and parameters). To assess the goodness of fit of the predicted circuit, we measure the distance between the impedance spectrum of the true circuit and the impedance spectrum of the predicted circuit. To measure the distance we use the mean absolute percentage error (MAPE) which is the relative version of the loss of the constraint optimization problem given in Eq. (7).

In the fitting problem in Eq. (7), we consider the spectra in the interval $f \in [10^{-6}, 10^8]$, which extends the frequency range $[10^{-3}, 10^8]$

Table 4
Benchmark results of our neural network model on different classification tasks and circuit models proposed in the literature. We show that our model outperforms other machine learning models on their classification task.

Classification task	Author's model	Author's accuracy	Our model's accuracy
5 Circuits [24]	Support Vector Machine	78%	98.8%
9 Circuits [21]	AdaBoost and Random Forest	58%	87.5%
3 Circuits, Scenario 1 [20]	Fully Connected Neural Network	95%	100%
3 Circuits, Scenario 2 [20]	Fully Connected Neural Network	75%	87%

Table 5
Regression and parameter fitting results for the true circuit impedance model and top 3 predicted circuit models from the neural network.

Method	Mean relative error [%]	Max relative error [%]
True Circuit	0.005%	1.57%
Predicted Circuit (1st)	0.05%	2.88%
Predicted Circuit (2nd)	1.16%	177%
Predicted Circuit (3rd)	4.7%	554%
Top-3 Prediction	0.005%	0.37%

that was used for predicting the topology by the neural network. By using this extended interval our metric is sensitive to circuit elements that only show significant effects in this smaller frequency range such as Warburg; if we would ignore the frequency range $[10^{-6}, 10^{-3}]$ some mathematically not equivalent circuits can still have a small error, which gives false indication on the neural network's performance.

Although the frequency range $f \in [10^{-6}, 10^{8}]$ is not practical due to the measurement time, the fitting error of a given circuit on the frequency $f \in [10^{-6}, 10^{8}]$ acts as an upper bound for the fitting error of frequency range $f \in [10^{-3}, 10^{8}]$.

Table 5 summarizes the mean relative errors. It shows that the fitting error of the 1st predicted circuit is low compared to the fitting error of the true circuit, which is in contrast to the bad top-1 accuracy of approximately 40%. A reason for this contrast is that the definition of accuracy ignores that different topologies can still be mathematically equivalent and thus have spectra with the same features.

In Fig. 6 we compare the top-3 fitting error (the minimum fitting error for the top-3 predictions) with the fitting error obtained for the circuit that was used for generating the spectra. The figure shows that the fitting error of the predicted and ground truth circuit are mostly close to the diagonal, or in other words, these errors are comparable. Since the fitting error of the true circuit is a quality metric for the optimization method, the comparability of the errors implies that the error of top-3 predicted circuit is to a large part explained by the optimization error. We can see in Fig. 6, that in a few cases, the fitting of the predicted circuit can have a lower error than that of fitting the ground truth circuit. This is, however, strictly an optimization error, where sometimes bad convergence occurs.

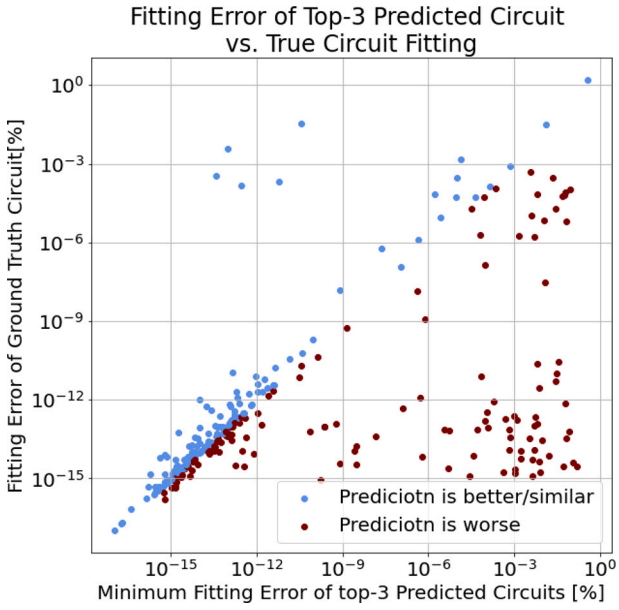

Fig. 6. Parameter fitting results of the top 3 predictions (the minimum fitting error of the top-3 predictions) of the neural network compared with the parameter fitting results of the true circuit evaluated on a data set of size 300. The fitting error is quantified as the mean absolute percentage error (MAPE). Note that, the fitting error of the ground-truth circuit is not exactly zero due to a limited amount of initial points in the multi-start optimization and limitations in floating-point precision.

5.3. Validation on measurement data

To validate the model against actual impedance experimental data, BDS was performed on two different polymer membranes (Nafion® 115 and Fumasep® FAA-3-PK-75, as reported in our previous work [26]). These two membranes were selected for their significance in the energy field, owing to their diverse mechanical, physical, and chemical properties, as well as their versatile applications. Nafion® 115 and Fumasep® FAA-3-PK-75 polymers, being widely used as cation- and anion-exchange membranes, contribute significantly to the performance and efficiency of (photo) electrolyzers, electrodialysis cells, and fuel cells operating in acidic and base environments, respectively. Hence, understanding the dielectric response of such polymer materials when subjected to electric fields is pivotal for optimizing the performance of various energy conversion technologies.

The measurement was done for both membranes over the frequency range $f \in [2 \times 10^{-1}, 10^{5}]$ with 70 measurement points each. Before identifying the equivalent electrical circuit with the impedance data obtained by the EIS measurement, it is essential to clean the data in order to minimize measurement errors and inaccuracies. Inaccuracies, especially at low frequencies, can result from different factors. Electrode polarization, for instance, can significantly impact the impedance measured at low frequencies, where the charge builds up at the electrode. Another important reason is Non-stationarity with respect to time, where measurements are not time-invariant anymore. This happens at low frequencies, where longer periods are required and thus changes in the system can happen within this time, for example, a rise in the system's temperature.

For instance, if the system being measured was non-stationary during the data collection process, large residuals could appear at lower frequencies [30].

For this reason, we are only interested in reliable frequency points and therefore the measurement data should comply with the principles of stationarity and time-invariance.

A reliable method that is often used in literature [30,31] for detecting irregularity in the measurement data is the Kramers–Kronig transformation [28]. This technique verifies that the EIS measurement points are stable and causal by analysing the relationship between the real and imaginary parts of the data. Conducting the Kramers–Kronig validation test shows that frequencies below 2 Hz are not reliable for both measurements for the reasons mentioned before. For this reason, we consider the frequencies down to 2 Hz only.

The neural network is then retrained on the newly generated data on the frequency range $f \in [2, 10^{5}]$.

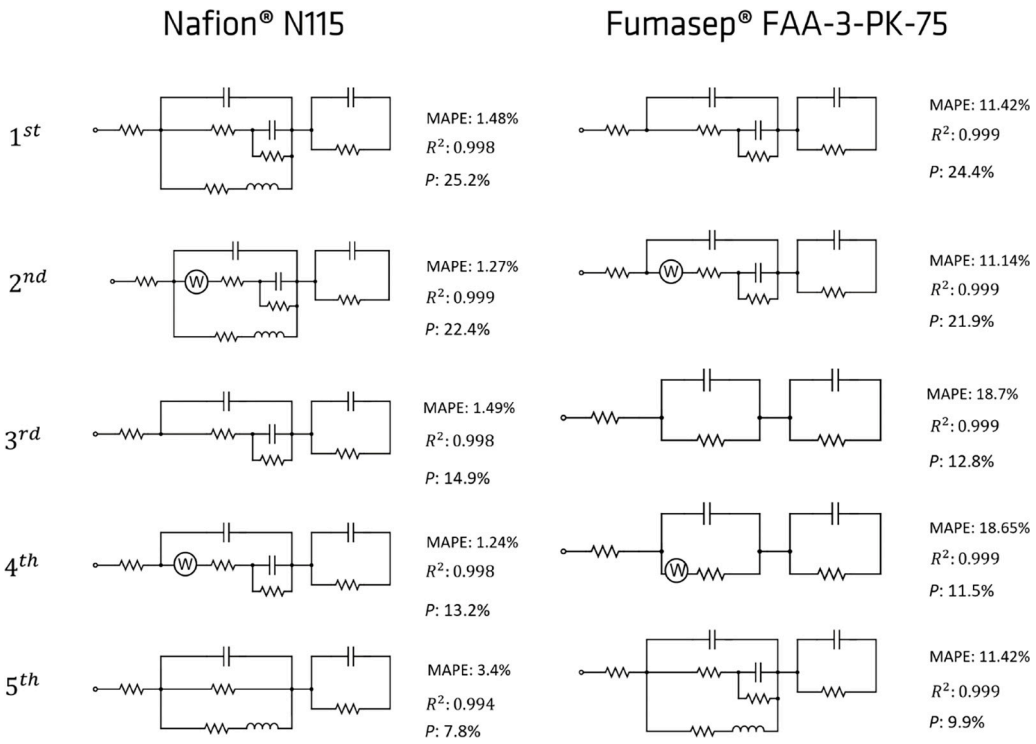

Fig. 7. The top-5 predictions of the neural network for Nafion® N115 (left) and Fumasep® FAA-3-PK-75 (right). The predicted circuits are ordered according to their probabilities. Moreover, beside each circuit, we show the fitting error, namely MAPE and R^2, in addition to their likelihood P (over the 96 possible circuits) predicted by the neural network.

In order to find the equivalent circuit we investigate the top five predictions of the neural network for each membrane. In Fig. 7 we show these predicted circuits ordered by their probabilities outputted by the neural network. Noteworthy, the R^2 for the five statistically most probable EECs for both membranes are very similar, if not identical. Therefore, selecting the final EEC is not trivial. Rather than providing a single EEC, we want to emphasize that our model should be used to predict a class of possible (and similar) EECs based on a statistical analysis conducted by the neural network. This will help the experimenter in minimizing the bias in the selection of the final EEC for the system under investigation. This selection should always be done by physically interpreting the EEC topology.

The selected EEC for both membranes from the five predictions can be seen in Fig. 8. The selection of the EEC has been conducted on the basis of the reported results in the literature [32]. To determine the parameters of the electrical elements for both membranes, we utilize the multi-start Trust Region method we introduced before. Additionally, to examine the uniqueness of the acquired minimas (parameters) by the optimizer, we repeat the fitting process multiple times. This yields three different parameter sets for Nafion® N115 and two different parameter sets for Fumasep® FAA-3-PK-75, which deliver the same fitting error values, 1.49% and 11.42%. The found sets of parameters for both membranes can be seen in Table 6. In Fig. 9, we show the mean impedance spectra resulting from the different sets of the parameters (Table 6) for both membranes, where the standard deviation for the different fits resulting from each set of parameters is 0.022 for Nafion® N115 and 0.033 for Fumasep® FAA-3-PK-75.

The error values obtained by fitting the selected EEC (Fig. 8), 1.49% and 11.42%, are larger compared with the error values that were acquired on the simulated data on the frequency range $f \in [10^{-3}, 10^{8}]$. The main reason for these error values is the fact that the mean absolute percentage error (MAPE) is very sensitive to variations at small values. For instance, high mean relative error values result when a small mismatch between the fit and the true curve at high frequencies where the values are small. It is also important to mention that if we consider another metric to measure the goodness of fit, namely the coefficient of determination R^2, we get a fit as good as 0.998 and 0.999 for Nafion® N115 and Fumasep® FAA-3-PK-75, respectively.

Table 6
Sets of parameters results from the fitting algorithm for the predicted circuit (Fig. 8) for both membranes Nafion® N115 and Fumasep® FAA-3-PK-75. The different sets of parameters found deliver the same error values and also the same impedance spectra (Fig. 9).

	Nafion® 115			Fumasep® FAA-3-PK-75	
	set 1	set 2	set 3	set 1	set 2
R_s [Ω]	2.4×10^2	2.4×10^2	2.4×10^2	2.8×10^2	2.8×10^2
R_1 [Ω]	5.8×10^2	70	2.2×10^2	1.15×10^3	1.95×10^4
R_{p1} [Ω]	77	1.08×10^2	3.9×10^2	2.01×10^4	8.03×10^3
C_p [F]	6.2×10^{-5}	4.4×10^{-5}	1.18×10^{-6}	2.8×10^{-6}	9.1×10^{-6}
C_1 [F]	1.4×10^{-6}	1.3×10^{-6}	7.1×10^{-7}	2.6×10^{-6}	2.57×10^{-6}
R_2 [Ω]	66	5.5×10^2	1.1×10^2	6.6×10^3	2.9×10^2
C_2 [F]	1.38×10^{-6}	1.47×10^{-6}	4.45×10^{-5}	5×10^{-6}	5.23×10^{-6}

Many other reasons influence the accuracy of predicting the equivalent circuit and its fitting. For instance, the frequency range of the measurement data $f \in [2, 10^5]$ is small and hence essential features are lost, which can worsen the performance of the neural network since the neural network was designed (including hyperparameters optimization) for impedance data that belongs to the frequency range $f \in [10^{-3}, 10^{8}]$.

Additionally, measurements are prone to noise and not ideal. This inherent factor introduces some deviation between the fit and the measurement since we are fitting an ideal function to the data.

Another critical reason for this deviation is the common practice of using the constant phase element for fitting equivalent circuits in EIS instead of capacitors. The constant phase element behaves similarly to a capacitor, however, it is still different. In this work, capacitors are used as proof of concept. Another important aspect that we want to highlight is the mutual correlation of the circuit elements, which is often overlooked. Thus, it is difficult to provide an unambiguous set of values for a given topology, independently of how the data analysis is conducted.

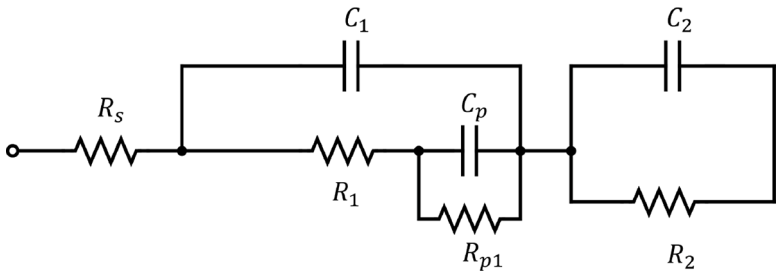

Fig. 8. The selected EEC from the top-5 predictions for both membranes.

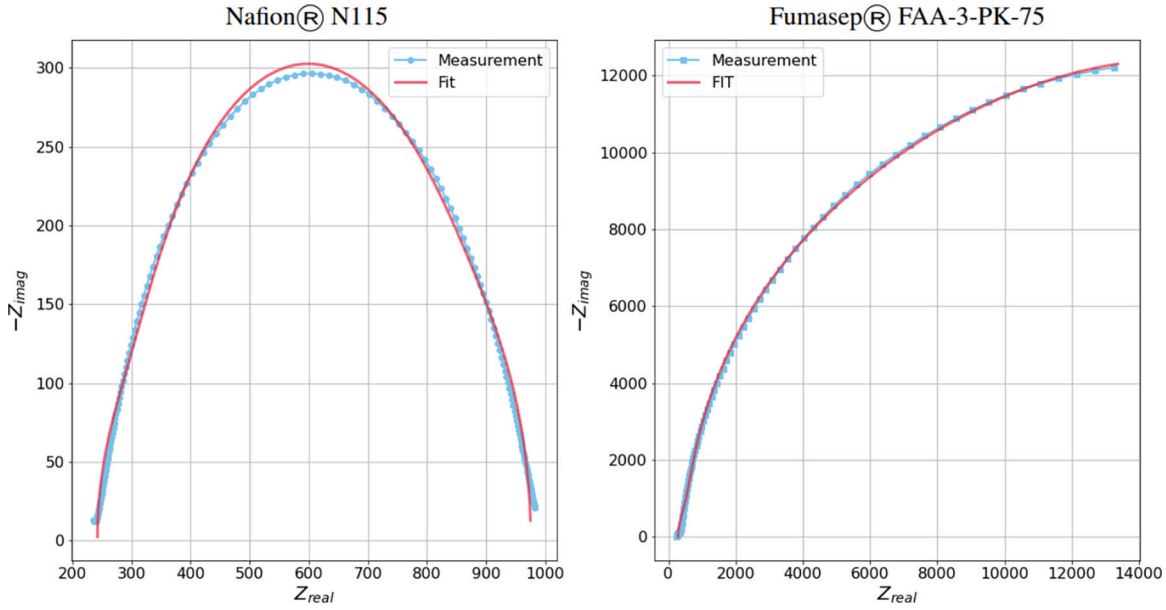

Fig. 9. The resulting mean spectra resulting from curve-fitting from the different sets of parameters found (Table 6) for both membranes with standard deviation values of 0.022 for Nafion® N115 and 0.033 for Fumasep® FAA-3-PK-75 for the spectra acquired by the different parameters sets. The mean curve-fitting of the different sets delivers the MAPE values of 1.49% and 11.42% and R^2 of 0.998 and 0.999 for Nafion® N115 (left) and Fumasep® FAA-3-PK-75 (right), respectively.

Regarding the physical interpretation of the EEC reported in Fig. 8, the presence of two main RC circuits can be observed: the first network, characterized by the presence of an RC in parallel with a capacitor, is ascribed to the mixed dielectric response of the membrane and the cell itself, as also reported previously [32]. Namely, the R_{p1}/C_p parallel describes the resistive/capacitive response of the membrane. Soboleva et al. [33] and Yadav et al. [34] have shown that the dielectric response of Nafion membranes can be described with a capacitance in parallel to a resistor that parametrizes the sheet or the bulk resistance of the polymer film, depending on the position of the probe electrodes. The origin of the membrane's capacitance has been described as the polarization of water in close proximity to the sulfonate groups inside the membrane's nanopores. Our neural network model showed that such a parameterization is valid for the Fumasep membrane as well. Hence, we propose that the capacitance exhibited by both polymer films (C_p) arises from the polarization of water in close proximity to the ionized functional groups present in the polymer's structure. The resistor R_{p1}, in our experimental setup, represents the polymer's sheet resistance. The R_1/C_1 parallel is instead due to the voltage probes contacting the sample under investigation, namely their interfacial resistance (R_1, similar values for both polymer samples) and double layer capacitance (C_1). The origin of the R_2/C_2 parallel is not clear. Interestingly, this parallel is present on all the five statistically relevant EECs, and for both membranes. The physical origin of this parallel is currently under investigation to determine if it can be attributed to eventual dielectric responses in the membranes neglected up to now in the literature. An alternative explanation is that the presence of this additional RC parallel could be due to the fact that ideal capacitors are used in the EEC, instead of constant phase elements (CPE). Finally, the serial resistance R_s originates partly from the contact between electrodes and probes and partly from the wire resistance [32].

6. Conclusion

In this work, we proposed a new neural network model that outperforms other machine learning models. By reducing user bias and enhancing data analysis, this approach aims to make BDS accessible to both experienced users and those with limited expertise. The combination of machine learning and BDS provides valuable insights into the dynamic behaviour of polymers and facilitates the design of tailored polymers for various applications. The proposed model achieves state-of-the-art results compared to other models and benchmarks, scoring a top-5 accuracy of around 80%. This model allows researchers to distinguish electrochemical processes in polymers that are difficult to identify through conventional data analysis of the experimental impedance data. Importantly, the model can also extrapolate beyond the measured frequencies, particularly for low frequencies where certain electrochemical processes, such as Warburg diffusion, become recognizable but are challenging or impractical to measure.

This approach significantly reduces the fitting time since researchers are not required to fit multiple circuits selected from an arbitrarily large search space. Instead, they can focus on the top predictions provided by the CNN. The proposed methodology not only delivers good results in terms of circuit search and fitting but also provides

a unified framework that addresses the issue of non-identifiability in material characterization, where circuit models are not unique [35]. This is due to the constrained search space of the universal circuit in addition to constraints on the regression problem (curve fitting). We also allow users to identify the most adequate circuit from the top-5 predictions when unique solutions are not available.

To further improve the neural network, hyperparameter optimization methods such as Bayesian optimization [36] can be conducted in addition to a CNN kernel size optimization methods [37], since the choice of the kernel size plays a major role in the overall performance of the model.

To validate the neural network performance on the actual experimental dielectric response of Nafion® N115 and Fumasep® FAA-3-PK-75 membranes, the neural network needed to be retrained. To address this issue, the frequency vector can be provided as an additional input to the CNN, and data can be generated on different frequency vectors to build a more flexible and adaptable model. Additionally, we have demonstrated that our model based on a CNN scores better than fully connected neural network models. This superiority arises from the ability of the CNN to exploit temporal features effectively, unlike fully connected models.

We want to highlight that, within our CNN model, it is important to regularize the optimization problem for parameter fitting to eliminate correlations between parameters and achieve physically meaningful results. Regularizing the neural network can also help address the issue of non-identifiability.

As an outlook of this work, we believe that investigating a Lasso regularized optimization method [23] for the regression part is worthwhile. This approach would introduce a Lasso regularization term (sparse regression) to the optimization algorithm for fitting the universal circuit. Such regularization would guide the optimization algorithm to parameterize the universal circuit to deliver the target topology by setting certain elements of the universal circuit to zero.

Another important step in building the proposed model is generating the impedance data. The data was generated on parameters sampled from a uniform distribution due to the lack of prior information on the true distribution. Conducting further studies on the distribution of parameters in dielectric spectroscopy can help achieve more accurate models that generalize well to real-life impedance measurements.

Finally, we want to highlight that our approach, although developed for dielectric spectroscopy of polymers, has broad applicability and can be effectively used in different fields of applications where dielectric spectroscopy is employed to characterize and understand the impedance response of the system under investigation.

CRediT authorship contribution statement

Bashar Albakri: Writing – original draft, Visualization, Software, Methodology, Formal analysis, Conceptualization. **Analice Turski Silva Diniz:** Investigation, Data curation. **Philipp Benner:** Writing – review & editing, Funding acquisition. **Thilo Muth:** Writing – review & editing, Funding acquisition. **Shinichi Nakajima:** Writing – review & editing, Validation, Supervision. **Marco Favaro:** Writing – original draft, Validation, Resources, Project administration, Funding acquisition, Conceptualization. **Alexander Kister:** Writing – review & editing, Validation, Supervision, Conceptualization.

Declaration of competing interest

The authors declare the following financial interests/personal relationships which may be considered as potential competing interests: Marco Favaro reports financial support was provided by Federal Ministry of Education and Research Berlin Office. Shinichi Nakajima reports financial support was provided by Federal Ministry of Education and Research Berlin Office. Marco Favaro reports financial support was provided by Friedrich Schiller University Jena. Marco Favaro reports financial support was provided by Helmholtz Center Berlin for Materials and Energy. Bashar Albakria reports financial support was provided by BAM Federal Institute for Materials Research and Testing. Philipp Benner reports financial support was provided by BAM Federal Institute for Materials Research and Testing. Thilo Muth reports financial support was provided by BAM Federal Institute for Materials Research and Testing. Alexander Kister reports financial support was provided by BAM Federal Institute for Materials Research and Testing. If there are other authors, they declare that they have no known competing financial interests or personal relationships that could have appeared to influence the work reported in this paper.

Data and code availability

The code supporting the findings of this study is openly available on GitHub at https://github.com/BAMeScience/EISNet, under MIT license. The repository includes detailed scripts used for generating, analysing, and processing the data involved in this study. All data required for replicating our published results are dynamically generated by these scripts. Users can refer to the README.md file in the repository for guidance on setting up the environment, running the scripts, and generating the data.

Acknowledgements

This project was partly supported by the Federal Ministry of Education and Research (BMBF) through the CatLab project (Förderkennzeichen 03EW0015 A) and BIFOLD - Berlin Institute for the Foundations of Learning and Data (01IS18025 A and 01IS18037 A). This project was also partially supported by the Helmholtz Institute for Polymers in Energy Applications (HIPOLE), jointly funded by the Friedrich Schiller University Jena and the Helmholtz-Zentrum Berlin. We would like to acknowledge Maryline Ralaiarisoa for her support in defining the cleaning/activation protocols of the polymer membranes experimentally investigated in this study, and Katrin Tietz and Thorsten Wagner for the fabrication of the membrane holder reported in this work.

References

[1] S. Peighambardoust, S. Rowshanzamir, M. Amjadi, Review of the proton exchange membranes for fuel cell applications, Int. J. Hydrog. Energy 35 (17) (2010) 9349–9384, http://dx.doi.org/10.1016/j.ijhydene.2010.05.017, URL https://www.sciencedirect.com/science/article/pii/S0360319910009523.

[2] W.H. Woodward, Broadband dielectric spectroscopy—A practical guide, in: Broadband Dielectric Spectroscopy: A Modern Analytical Technique, ACS Publications, 2021, pp. 3–59.

[3] J. Garcia-Navarro, M. Isaacs, M. Favaro, D. Ren, W.-J. Ong, M. Grätzel, P. Jiménez-Calvo, Updates on hydrogen value chain: A strategic roadmap, 2023.

[4] G. Segev, J. Kibsgaard, C. Hahn, Z.J. Xu, T.G. Deutsch, C. Xiang, J.Z. Zhang, L. Hammarström, D.G. Nocera, A.Z. Weber, et al., The 2022 solar fuels roadmap, J. Phys. D: Appl. Phys. 55 (32) (2022) 323003.

[5] G.A. Lindquist, Q. Xu, S.Z. Oener, S.W. Boettcher, Membrane electrolyzers for impure-water splitting, Joule 4 (12) (2020) 2549–2561, http://dx.doi.org/10.1016/j.joule.2020.09.020, URL https://www.sciencedirect.com/science/article/pii/S2542435120304566.

[6] S. Suriyakumar, P. Bhardwaj, A.N. Grace, A.M. Stephan, Role of polymers in enhancing the performance of electrochemical supercapacitors: A review, Batteries Supercaps 4 (4) (2021) 571–584.

[7] S. Ahmed, P. Sharma, S. Bairagi, N.P. Rumjit, S. Garg, A. Ali, C.W. Lai, S.M. Mousavi, S.A. Hashemi, C.M. Hussain, Nature-derived polymers and their composites for energy depository applications in batteries and supercapacitors: Advances, prospects and sustainability, J. Energy Storage 66 (2023) 107391, http://dx.doi.org/10.1016/j.est.2023.107391, URL https://www.sciencedirect.com/science/article/pii/S2352152X23007880.

[8] J. Ravi, M.H.D. Othman, T. Matsuura, M. Ro'il Bilad, T. El-badawy, F. Aziz, A. Ismail, M.A. Rahman, J. Jaafar, Polymeric membranes for desalination using membrane distillation: A review, Desalination 490 (2020) 114530, http://dx.doi.org/10.1016/j.desal.2020.114530, URL https://www.sciencedirect.com/science/article/pii/S0011916419323951.

[9] K.D. Rao, S. Tunga, Signals and Systems, Springer, 2018.

[10] V. Vivier, M.E. Orazem, Impedance analysis of electrochemical systems, Chem. Rev. 122 (12) (2022) 11131–11168.

[11] S. Fletcher, Tables of degenerate electrical networks for use in the equivalent-circuit analysis of electrochemical systems, J. Electrochem. Soc. 141 (7) (1994) 1823, http://dx.doi.org/10.1149/1.2055011.
[12] A.C. Lazanas, M.I. Prodromidis, Electrochemical impedance spectroscopy–A tutorial, ACS Measur. Sci. Au (2023).
[13] M.J. Powell, A hybrid method for nonlinear equations, in: Numerical Methods for Nonlinear Algebraic Equations, Gordon and Breach, 1970, pp. 87–161.
[14] M.D. Murbach, B. Gerwe, N. Dawson-Elli, L. kun Tsui, impedance.py: A Python package for electrochemical impedance analysis, J. Open Source Softw. 5 (52) (2020) 2349, http://dx.doi.org/10.21105/joss.02349.
[15] N. Tian, Y. Wang, J. Chen, H. Fang, On parameter identification of an equivalent circuit model for lithium-ion batteries, in: 2017 IEEE Conference on Control Technology and Applications, CCTA, IEEE, 2017, pp. 187–192.
[16] F. Pizzitutti, F. Bruni, Electrode and interfacial polarization in broadband dielectric spectroscopy measurements, Rev. Sci. Instrum. 72 (5) (2001) 2502–2504.
[17] A.J. Bae, C. Beta, E. Bodenschatz, Rapid switching of chemical signals in microfluidic devices, Lab Chip 9 (21) (2009) 3059–3065.
[18] R. Lillard, P. Moran, H. Isaacs, A novel method for generating quantitative local electrochemical impedance spectroscopy, J. Electrochem. Soc. 139 (4) (1992) 1007.
[19] V.M. Huang, S.-L. Wu, M.E. Orazem, N. Pébère, B. Tribollet, V. Vivier, Local electrochemical impedance spectroscopy: A review and some recent developments, Electrochim. Acta 56 (23) (2011) 8048–8057.
[20] V. Bongiorno, S. Gibbon, E. Michailidou, M. Curioni, Exploring the use of machine learning for interpreting electrochemical impedance spectroscopy data: Evaluation of the training dataset size, Corros. Sci. 198 (2022) 110119.
[21] Z. Zhao, Y. Zou, P. Liu, Z. Lai, L. Wen, Y. Jin, EIS equivalent circuit model prediction using interpretable machine learning and parameter identification using global optimization algorithms, Electrochim. Acta 418 (2022) 140350.
[22] A. Al-Ali, B. Maundy, A. Allagui, A. Elwakil, Optimum impedance spectroscopy circuit model identification using deep learning algorithms, J. Electroanal. Chem. 924 (2022) 116854.
[23] S. Buteau, J.R. Dahn, Analysis of thousands of electrochemical impedance spectra of lithium-ion cells through a machine learning inverse model, J. Electrochem. Soc. 166 (8) (2019) A1611, http://dx.doi.org/10.1149/2.1051908jes.
[24] S. Zhu, X. Sun, X. Gao, J. Wang, N. Zhao, J. Sha, Equivalent circuit model recognition of electrochemical impedance spectroscopy via machine learning, J. Electroanal. Chem. 855 (2019) 113627.
[25] J. Schaeffer, P. Gasper, E. Garcia-Tamayo, R. Gasper, M. Adachi, J.P. Gaviria-Cardona, S. Montoya-Bedoya, A. Bhutani, A. Schiek, R. Goodall, et al., Machine learning benchmarks for the classification of equivalent circuit models from electrochemical impedance spectra, J. Electrochem. Soc. 170 (6) (2023) 060512.
[26] M. Ralaiarisoa, S.S. Krishnamurti, W. Gu, C. Ampelli, R. van de Krol, F.F. Abdi, M. Favaro, In situ investigation of ion exchange membranes reveals that ion transfer in hybrid liquid/gas electrolyzers is mediated by diffusion, not electromigration, J. Mater. Chem. A 11 (25) (2023) 13570–13587.
[27] A.R. Bredar, A.L. Chown, A.R. Burton, B.H. Farnum, Electrochemical impedance spectroscopy of metal oxide electrodes for energy applications, ACS Appl. Energy Mater. 3 (1) (2020) 66–98.
[28] B.A. Boukamp, A linear Kronig-Kramers transform test for immittance data validation, J. Electrochem. Soc. 142 (6) (1995) 1885.
[29] P. Virtanen, R. Gommers, T.E. Oliphant, M. Haberland, T. Reddy, D. Cournapeau, E. Burovski, P. Peterson, W. Weckesser, J. Bright, S.J. van der Walt, M. Brett, J. Wilson, K.J. Millman, N. Mayorov, A.R.J. Nelson, E. Jones, R. Kern, E. Larson, C.J. Carey, İ. Polat, Y. Feng, E.W. Moore, J. VanderPlas, D. Laxalde, J. Perktold, R. Cimrman, I. Henriksen, E.A. Quintero, C.R. Harris, A.M. Archibald, A.H. Ribeiro, F. Pedregosa, P. van Mulbregt, SciPy 1.0 Contributors, SciPy 1.0: Fundamental Algorithms for Scientific Computing in Python, Nature Methods 17 (2020) 261–272, http://dx.doi.org/10.1038/s41592-019-0686-2.
[30] S. Bauknecht, J. Kowal, B. Bozkaya, J. Settelein, E. Karden, Electrochemical impedance spectroscopy as an analytical tool for the prediction of the dynamic charge acceptance of lead-acid batteries, Batteries 8 (7) (2022) 66.
[31] B.A. Boukamp, Practical application of the kramers-kronig transformation on impedance measurements in solid state electrochemistry, Solid State Ion. 62 (1–2) (1993) 131–141.
[32] D.K. Paul, R. McCreery, K. Karan, Proton transport property in supported Nafion nanothin films by electrochemical impedance spectroscopy, J. Electrochem. Soc. 161 (14) (2014) F1395.
[33] T. Soboleva, Z. Xie, Z. Shi, E. Tsang, T. Navessin, S. Holdcroft, Investigation of the through-plane impedance technique for evaluation of anisotropy of proton conducting polymer membranes, J. Electroanal. Chem. 622 (2) (2008) 145–152.
[34] R. Yadav, P.S. Fedkiw, Analysis of EIS technique and Nafion 117 conductivity as a function of temperature and relative humidity, J. Electrochem. Soc. 159 (3) (2012) B340.
[35] V. Vivier, M.E. Orazem, Impedance analysis of electrochemical systems, Chem. Rev. 122 (12) (2022) 11131–11168, http://dx.doi.org/10.1021/acs.chemrev.1c00876, PMID: 35687869.
[36] M. Balandat, B. Karrer, D. Jiang, S. Daulton, B. Letham, A.G. Wilson, E. Bakshy, BoTorch: A framework for efficient Monte-Carlo Bayesian optimization, in: H. Larochelle, M. Ranzato, R. Hadsell, M. Balcan, H. Lin (Eds.), in: Advances in Neural Information Processing Systems, vol. 33, Curran Associates, Inc., 2020, pp. 21524–21538.
[37] W. Tang, G. Long, L. Liu, T. Zhou, J. Jiang, M. Blumenstein, Rethinking 1D-CNN for time series classification: A stronger baseline, 2020, pp. 1–7, arXiv preprint arXiv:2002.10061.